Multi-dimensional Simulations of the Solar Wind and Interplanetary Coronal Mass Ejections

Han Zhang

A thesis submitted in fulfilment of the requirements for the degree of MSc in Physics and the Diploma of Imperial College London

September 3rd, 2019

Abstract

The space weather is gaining its importance in modern society, and it is tightly linked to the solar activities in the inner heliosphere. There are two main parts of those activities: the solar wind and the extreme interplanetary coronal mass ejections(ICMEs). Understanding those phenomena is significant for forecasting the space weather, and it is a rather active research area within space physics. In this project, we simulate the propagation of the solar wind and extreme CMEs through the inner heliosphere using the astrophysical fluid dynamics code **PLUTO** and the Imperial high performance computing system. The code shows the potential for space weather forecast compared to other solar wind simulation models. Then as a case study, we investigate a modern-era extreme event which happened on 23 July 2012 in both hydrodynamics(HD) and magnetohydrodynamics(MHD). The result provides insight into the mechanism behind the formation of the extreme CMEs.

Contents

Declaration of the work

Except for the core **PLUTO** code, I wrote all the code in this project, including data I/O, initial and boundary condition setting and synthetic satellite plot generation. The all other parts of this project are completed by myself.

Acknowledgement

1 Introduction

The space weather of the earth is mainly controlled by solar activities in the inner heliosphere. As a mid-age main-sequence star, the Sun ejects a large amount of mass via high-velocity plasma flow every second, which forms the ambient part of the heliosphere environment: the solar wind. The solar wind mainly contains the protons and electrons, as well as some alpha particles(Meyer-Vernet, 2007). Those particles come from the outer atmosphere of the Sun known as the corona, and gain pretty high energy due to an unexplained heating phenomenon(Chen et al., 2019). The solar wind accelerates to supersonic speed within several radii away from the Sun, and the speed typically varies from 250km/s to 750km/s which depends on the latitude and longitude it launches and the time in the solar cycle. Figure 1 shows the speed of the solar wind as a function of launch latitude during solar minimum and maximum. The solar wind could roughly be divided into the slow and fast solar wind. During the solar minimum, slow solar wind is mainly emitted in low latitude region named "streamer belt", where the magnetic field that extends from the corona forms closed loop. It is usually denser and has a more complicated structure compared to its fast counterpart. The typical velocity and temperature of slow solar wind when it arrives earth are $300-500$km/s and 10^5K. The fast solar wind, on the other hand, is launched in the region near the poles where the magnetic fields lines are open to the space. Near the earth, the velocity of fast solar wind is measured to be around 750km/s and the temperature to be 8×10^5km/s(Meyer-Vernet, 2007). When the solar maximum comes, the slow and fast solar wind do not have clear emitting patterns, and they may launch together in the same region sometimes. This could be seen quite clearly in figure 1.

The solar wind also carries the interplanetary magnetic field with it(Owens and Forsyth, 2013). Given the high electrical conductivity of the solar wind, the plasma flow of it could be treated as an ideal MHD fluid, where the frozen-in theorem applies. That means the plasma would carry the magnetic field with it and the topology of the magnetic lines does not change during the propagation in the heliosphere. Due to the combination of the outward motion of the solar wind and the self-rotation of the Sun, the plasma flow in the heliosphere from the sun follows an Archimedean spiral, which leads to a similar magnetic field lines structure known as Parker Spiral. It has its name from the American solar astrophysicist Eugene Newman Parker, who developed the model for the supersonic solar wind and predicted the spiral pattern of the interplanetary magnetic field in the solar system during the 1950s(Parker, 1965). Based on the polarity at the foot point on the Sun's surface, the interplanetary magnetic field lines point either outward or inward. This generates a current sheet (the Heliospheric Current Sheet, HCS) that separates the magnetic field with opposite direction. The sheet co-rotates with the solar wind and the offset between solar magnetic dipoles and rotation axis make it warp into a complicate shape sometimes called "the ballerina skirt" (See figure 2). The shape of the HCS will change with a period of the solar cycle for the polarity of the Sun reverses every 11 years(Thomas and Smith, 1981).

The interaction between the solar wind and magnetic fields forms the main part of space weather. With the boundary of a magnetopause, the magnetic field of the earth protects against the solar wind and forms a magnetic cavity known as a magnetosphere. However, this protection is far from perfect, as the environment inside the magnetosphere heavily depends on the property of the solar wind and interplanetary magnetic field it carries. The change in velocity, field direction and density of solar wind may lead to ionization or shrinking and expansion of the magnetopause for several earth radii(Russell et al., 1990), which threatens satellites and power grids on the earth. That makes the solar wind essential in the study of the space weather.
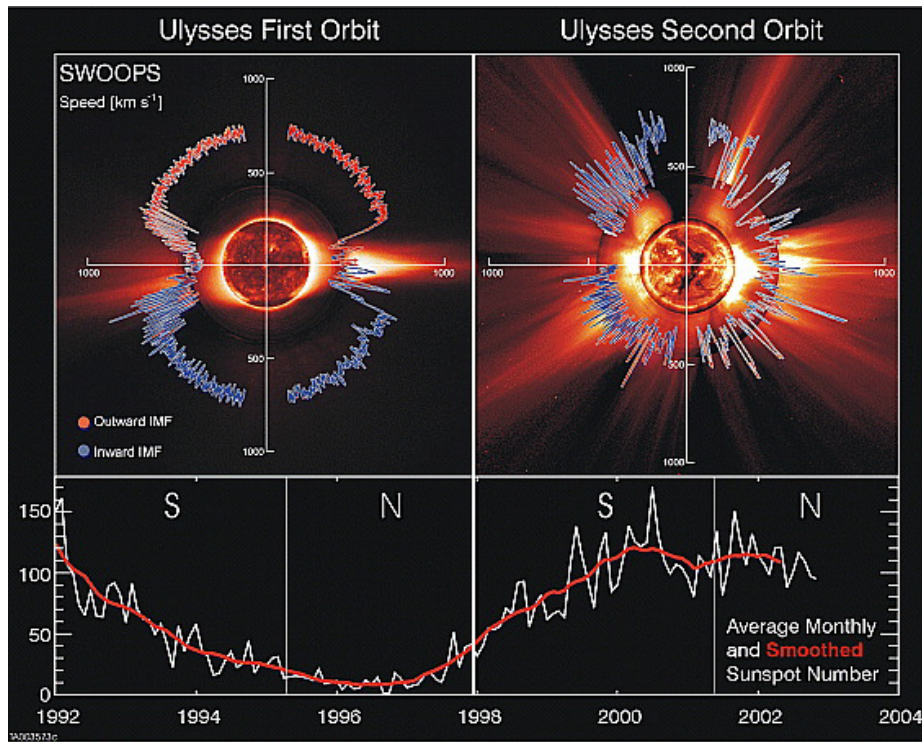
Figure 1: The velocity of the solar wind as a function of latitude. The data is from the two orbits of satellite *Ulysses*. The sunspot count in the lower panel indicates the first orbit is in solar minimum and the second in the second orbit in solar maximum. Taken from McComas et al. (2003).
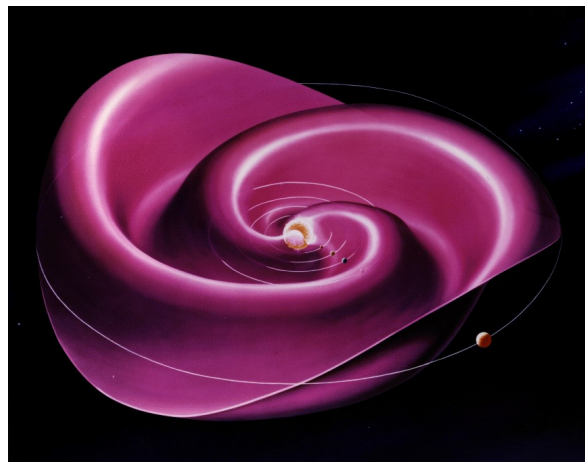

Figure 2: The wavy shape of the heliospheric current sheet. Taken from WSO archive.

Another important phenomenon affecting space weather is interplanetary coronal mass ejections. The CME is characterised as the great and explosive eruption of plasma from the solar corona, which contains a much stronger magnetic fields compared to the background solar wind. The plasma flow and the embedded magnetic field propagate into the heliosphere at speeds ranging from 100km/s to nearly 3000km/s (Hundhausen et al., 1994) and arrive at earth in one or several days. Though the precise initiation process of CME is still unclear, it is widely believed that the energy source of the CME is magnetic reconnection in the corona(Savage et al., 2010), where considerable energy stored in the magnetic field releases via erupted materials during this process. The mass of the ejected plasma can reach the order of 10^{15}-10^{16} g with the energy of $10^{31} - 10^{32}$ ergs(Manchester et al., 2006). During solar maximum, the Sun generates about three CME in a day, while during solar minimum the frequency decreases to about one CME every five days(Kahler, 1992).

The morphology of the CME could be observed in Thomason-scattered white-light via coronagraph(Manchester et al., 2017), in which the brightness shows the electron (thus the plasma) density. Because many factors may affect the evolution of CME from initiation, the CME morphologies have a great variation. The simplest structure of CME includes three parts: a bright leading front, a dark cavity of low-density, and a high-density core. This fundamental structure can remain and propagate into the heliosphere, and could also be seen in some active region in the corona, which is regarded as the progenitor of CME(van Driel-Gesztelyi and Culhane, 2009).
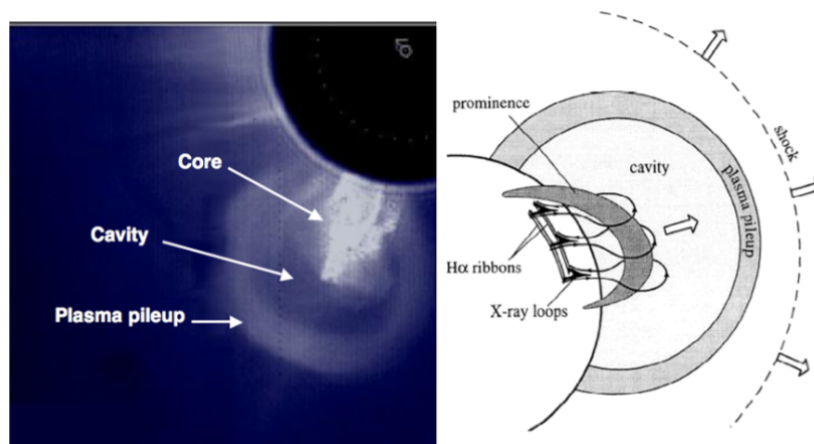

Figure 3: Left panel: A Solar Maximum Mission(MacQueen et al., 1980) archived image showing "classic" coronal mass ejection structure. Right panel: An illustration of CME features. Taken from van Driel-Gesztelyi and Culhane (2009).

Though most CMEs travel in a speed comparable to the ambient solar wind, there are some cases when it propagates into heliosphere at extremely high speed over one or two thousand kilometres per second. Those CME are called "extreme events", whose frequency of occurrence is believed to follow a power law distribution(Riley et al., 2011). While they are rare events, those extreme events have a great influence on space weather. Producing a shock wave ahead of it, the extreme ICMEs interact with the day-side magnetosphere of the earth and generate geomagnetic storms. By pushing the magnetopause towards the earth significantly, the storms could destroy satellites

hardware, cause the large-scale electrical blackouts and block the long-range radio communication. It also poses a threat to the navigation system, animals, and also to astronauts in space(Gonzalez et al., 1994).

the most famous extreme ICME is known as the Carrington Event in 1859, which struck the earth in 17.6 hours with a speed over 2000km/s(Tsurutani et al., 2003). The corresponding flares were recorded by the British astronomer Richard C. Carrington and Richard Hodgson(Carrington, 1859). This ICME induced one of the largest geomagnetic storms on record, which shut down the whole telegraph system over Europe and North America and produced aurora seen all over the world, even near the equator like Colombia. Several extreme ICMEs with strength comparable to the Carrington ones are reported by space satellites in recent years, like ones in 2003 October and November(known as Halloween Events) by SOHO(Manchester et al., 2008), and the one in 2012 July 23 by STEREO(Riley et al., 2016).

Given the complicated magnetogram on the surface of the Sun and the magnetohydrodynamics character of the solar wind and ICMEs, the purely theoretical analysis of them usually has many difficulties(Forbes et al., 2006). In later 1990s, the introduction of the massive-parallel supercomputer made the accurate three-dimensional MHD simulations possible, and the simulations gain increased importance these years as a powerful tool to bridge theories and observations and in forecasting the space weather.

As a gentler and more hydrodynamics-like phenomenon, the solar wind is easier to theoretically analyse and simulate. In the past two decades, several models have been developed for the solar wind like AWSoM(van der Holst et al., 2014), **ENLIL**(Odstrcil, 2003) and **EUHFORI-A**(Pomoell and Poedts, 2018). Those models usually consist of a corona part and heliosphere part, which use different assumptions while solving the differential equations of MHD. The ENLIL is the most famous heliosphere model for the solar wind simulation, with its cooperated corona model **WSA**(Parsons et al., 2011) or **MAS**. It is used by NASA Space Weather Research Center(SWRC) for space weather forecasting and works well for the solar wind.

On the other hand, however, the MHD simulation of the CME is much more complicated. Based on the theoretical model proposed by Gibson and Low (1998), most simulations of CME use twisted flux rope as magnetic structure within the plasma cavity, which has its root on the surface of the Sun. The self-like expansion of the rope could successfully reproduce many observational features of certain CME events, including the deceleration and acceleration during propagation, the structure of the magnetic field in ICMEs, and the observed morphology(Manchester IV et al., 2004; Manchester et al., 2008; Wood and Howard, 2009). However, this model requires a huge amount of calculation resources and is not realistic to implement in the real-time space weather forecast. Therefore, some simplifications are adopted in models currently used in forecasting. For example, the ENLIL-Cone model the SWRC uses treat CME as a cone with constant angular and radial velocity, and do not specify magnetic structure. These quasi-hydrodynamics methods are also used by the EUHFORIA. These simplifications result in a just passable precision(Mays et al., 2015). Further development in computational power/optimised algorithm and in the accuracy of simulation models are required, before a complete and practical MHD forecast system could be put into use.

The remaining part of the article proceeds as follows: The Section 2 we introduce the code **PLUTO** we used in our project and its HD and MHD module; In section 3 a complete collection of simulations are given, divided into three categories. We investigated the specific ICME event on July 2012 as the case study in section 4. Finally, we gave a brief discussion and conclusion in section 5.
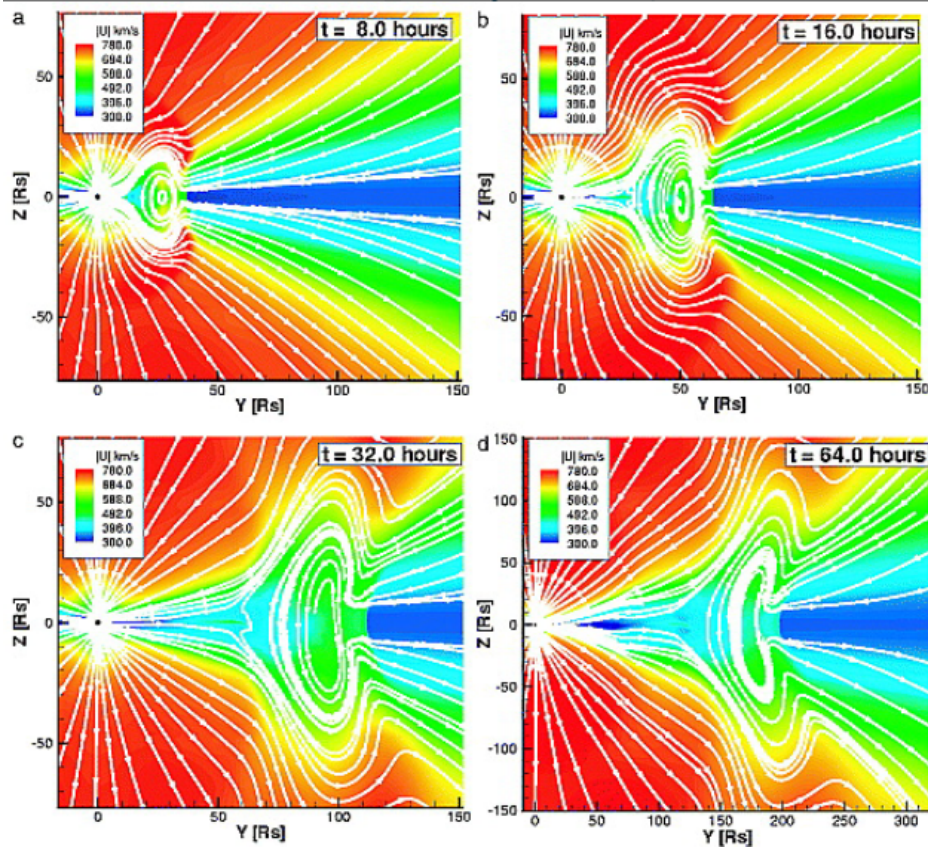
Figure 4: An example of CME simulation in the y-z meridional plane using flux rope model at a)t=8 hours b)t=16 hours c)t=32 hours d)t=64 hours. The solid white lines represent magnetic field lines, and the distribution of velocity is shown in the false-colour diagram. Taken from Manchester IV et al. (2004).

2   The PLUTO code and Methods

The core simulation code we use in this project is **PLUTO**, a special designed code for high mach plasma fluid(Mignone et al., 2007) which is perfect for the work on the solar wind and ICMEs. It solves partial differential equations from conservation laws in the form of

$$\frac{\partial \boldsymbol{U}}{\partial t} = -\nabla \cdot \mathbf{T}(\boldsymbol{U}) + \boldsymbol{S}(\boldsymbol{U}) \tag{1}$$

Here the $\boldsymbol{U}$ is a state vector of conservative quantities, $\mathbf{T}$ is a tensor denotes the flux of the each component of state vector. $\mathbf{S}$ defines the source terms. A great advantage of the code is that the general integration sequence does not require the explicitly forms of $\mathbf{U}, \mathbf{T}$ and $\mathbf{S}$, which leads to a flexibility in using different physics modules. **PLUTO** supports simulation in HD, MHD, relativistic HD(RHD) and RMHD. In this project, the HD and MHD modules are used, as

Solar wind and ICME is strongly non-relativistic. The code also provide various options including coordinate systems, rotation frame and particle compositions, which is relatively straight forward to implement.

In the HD modules, the stat vector and flux tensor **PLUTO** use are

$$U = \begin{pmatrix} \rho \\ \boldsymbol{m} \\ E \end{pmatrix}, \quad \mathbf{T}(U) = \begin{pmatrix} \rho\boldsymbol{v} \\ \boldsymbol{m}\boldsymbol{v} + p\mathbf{I} \\ (E+p)\boldsymbol{v} \end{pmatrix}^T \tag{2}$$

Including the source term, it leads to the conservation equations as

$$\frac{\partial}{\partial t} \begin{pmatrix} \rho \\ \mathbf{m} \\ E_t + \rho\Phi \end{pmatrix} + \nabla \cdot \begin{pmatrix} \rho\boldsymbol{v} \\ \boldsymbol{m}\boldsymbol{v} + p\mathbf{I} \\ (E_t + p + \rho\Phi)\,\boldsymbol{v} \end{pmatrix}^T = \begin{pmatrix} 0 \\ -\rho\nabla\Phi + \rho\boldsymbol{g} \\ \boldsymbol{m}\cdot\boldsymbol{g} \end{pmatrix} \tag{3}$$

The $\mathbf{m}$ here is the momentum density term equal to $\rho\mathbf{v}$, $\mathbf{I}$ is the unit three dimensional tensor. ϕ and $\mathbf{g}$ are the potential part and vector part of the body force. They belong to the source term. p is the thermal pressure and E_t is the total energy given by

$$E_t = \rho e + \frac{\boldsymbol{m}^2}{2\rho} \tag{4}$$

where e is the internal energy. An equation of state shall be provide for closure with a form of $\rho e = \rho e(p, \rho)$. Particularly, for an ideal gas closure, it satisfies

$$\rho e = \frac{p}{\Gamma - 1} \tag{5}$$

Other symbols not specified have their usual meanings.

In the MHD module, the conservation equations are extended to include the magnetic field, the state vector and flux tensor for this module are

$$U = \begin{pmatrix} \rho \\ \boldsymbol{m} \\ \boldsymbol{B} \\ E \end{pmatrix}, \mathbf{T}(U) = \begin{bmatrix} \rho\boldsymbol{v} \\ \boldsymbol{m}\boldsymbol{v} - \boldsymbol{B}\boldsymbol{B} + p_t\mathbf{I} \\ \boldsymbol{v}\boldsymbol{B} - \boldsymbol{B}\boldsymbol{v} \\ (E + p_t)\,\boldsymbol{v} - (\boldsymbol{v}\cdot\boldsymbol{B})\boldsymbol{B} \end{bmatrix}^T \tag{6}$$

Here $p_t = p + |\mathbf{B}|^2/2$ is the total (thermal plus magnetic) pressure. With the source term, they give the partial differential equation as

$$\frac{\partial \rho}{\partial t} + \nabla \cdot (\rho\mathbf{v}) = 0$$

$$\frac{\partial \mathbf{B}}{\partial t} + \nabla \times (c\mathbf{E}) = 0$$

$$\frac{\partial \mathbf{m}}{\partial t} + \nabla \cdot \left[\mathbf{m}\boldsymbol{v} - \mathbf{B}\mathbf{B} + \mathbf{I}\left(p + \frac{B^2}{2}\right)\right]^T = -\rho\nabla\Phi + \rho\mathbf{g} \tag{7}$$

$$\frac{\partial\,(E_t + \rho\Phi)}{\partial t} + \nabla \cdot [(E + p_t)\,\boldsymbol{v} + c\boldsymbol{E} \times \boldsymbol{B}] = \boldsymbol{m}\cdot\boldsymbol{g}$$

Most symbols have similar meanings to the HD part, while a magnetic term is added to the total energy

$$E_t = \rho e + \frac{\boldsymbol{m}^2}{2\rho} + \frac{\boldsymbol{B}^2}{2} \tag{8}$$

For an ideal state equation it has $\rho e = p/\Gamma - 1$ as well. The generalised Ohm's law can be written as

$$c\boldsymbol{E} = -\boldsymbol{v} \times \boldsymbol{B} + \frac{\eta}{c} \cdot \boldsymbol{J} + \frac{\boldsymbol{J}}{ne} \times \boldsymbol{B} \quad (\boldsymbol{J} = c\nabla \times \boldsymbol{B}) \tag{9}$$

The second term is the resistive term with η the resistivity tensor, and the third term comes from Hall effect. In the ideal case (where the report based), only the first term is retained.

To satisfy the Maxwell equation $\nabla \cdot \mathbf{B} = 0$, the Eight-Wave formulation is assigned(Powell et al., 1999), where an extra term is added to the right side of equation 7:

$$\frac{\partial}{\partial t} \begin{pmatrix} \rho \\ \mathbf{m} \\ E_t \\ \mathbf{B} \end{pmatrix} + \nabla \cdot (\ldots) = -\nabla \cdot \mathbf{B} \begin{pmatrix} 0 \\ \mathbf{B} \\ \mathbf{v} \cdot \mathbf{B} \\ \mathbf{v} \end{pmatrix} \tag{10}$$

This simulation project started with several test problems provided by the **PLUTO** package itself to check if the code is correctly compiled and executed, then we move to the simulation of the solar wind and ICMEs, start from one dimension then to two and three dimensions.

For the first stage of simulation, the general idea is to assign the boundary conditions and initial conditions by hand, hoping to recreate the structure of the steady-state solar wind and ICMEs. We implement a simple one dimensional simulation for an ICME as an initial step, with a uniformed-distributed, constant speed background solar wind. Then we examined the two-dimensional simulations in Earth rotation plane$(r - \phi)$ and the vertical plane$(r - \theta)$, followed by a general three-dimensional simulation. A simplified source boundary is assigned counting in the different launched regions of slow solar wind and fast solar wind, which is shown in figure 5. For the two dimensional cases, a cut through this boundary is used.

In the second stage, we try to input the boundary condition from data of other models to test the potential in space forecast of the code. In this project, we used the boundary data of **ENLIL**, which gives the density, temperature, three components of velocity and three components of the magnetic field on the inner boundary. **PLUTO** showed good flexibility to adopt the boundary data and the ability to be data-driven. In particular, we simulate the realistic solar wind background on July 2012, in which period an extreme ICMEs was recorded. By launched ICMEs in the ambient solar wind, we investigated the mechanism behind its extreme property. The reader can refer to the section of the case study for more information.

One point should be specified that, as a heliosphere simulation without a corona region, it is pretty hard to include any detailed structure of the magnetic field of ICMEs. So in our study, the quasi-hydrodynamics method is used like the models we mentioned above. Instead of any analytical structure, we enhanced the strength of the magnetic field by several times and left the direction unchanged. The pure hydrodynamics simulation of the 2012 July events is also given in the case study.

As a quite thin plasma with a density of only dozens of protons per cube centimetre, we dropped most of the non-ideal effects like resistivity, Hall effect but the adiabatic index γ. We hope to use a smaller γ to represent the alpha particles composition in the solar wind and ICMEs, and for a
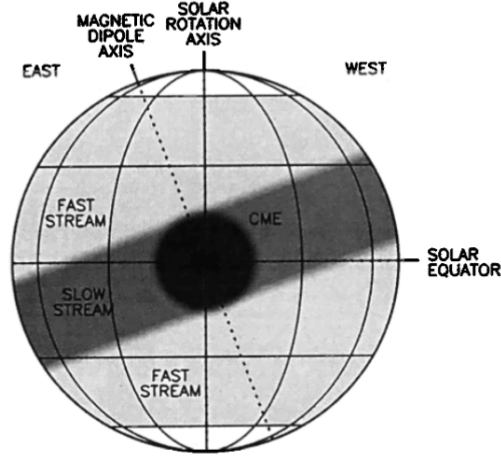
Figure 5: The source boundary surface used in the simulation. The slow solar wind is launched in the low latitude region while fast solar wind launch in the higher latitude. For parameter and mathematical expression of the boundary, please refer to the next section. Taken from Odstrcil and Pizzo (1999).

more gentle temperature gradient (which comes from the "solar wind heating") in the simulation domain.

3 The Simulation Results

This section shows the collection of simulation results and any specified condition and assumption we used in the study. For the clarity, All the simulations are labeled from **SIMU1** to **SIMU6**.

Please be aware that code units are used here for a stable simulation. We set unit length as solar radius(7×10^5km), unit density as $20 M_p/\mathrm{cm}^3$ where M_p is the mass of proton, unit velocity as 100km/s. Other quantities could be deduced from the three above:

$$
\begin{aligned}
B_U &= \sqrt{4\pi \rho_U} v_U = 2 \times 10^{-4} \mathrm{Gauss} \\
P_U &= \rho_U * v_U^2 = 3.2 \times 10^{-9} \mathrm{Pa} \\
T_U &= \frac{L_U}{v_U} = 7000\mathrm{s} \approx 1.95 \mathrm{hour}
\end{aligned}
\tag{11}
$$

Some plots in this paper may use code unit on the axes.

3.1 The Initial Simulations

The first two simulations are more fundamental but also reveal several important properties of the solar wind and ICMEs.
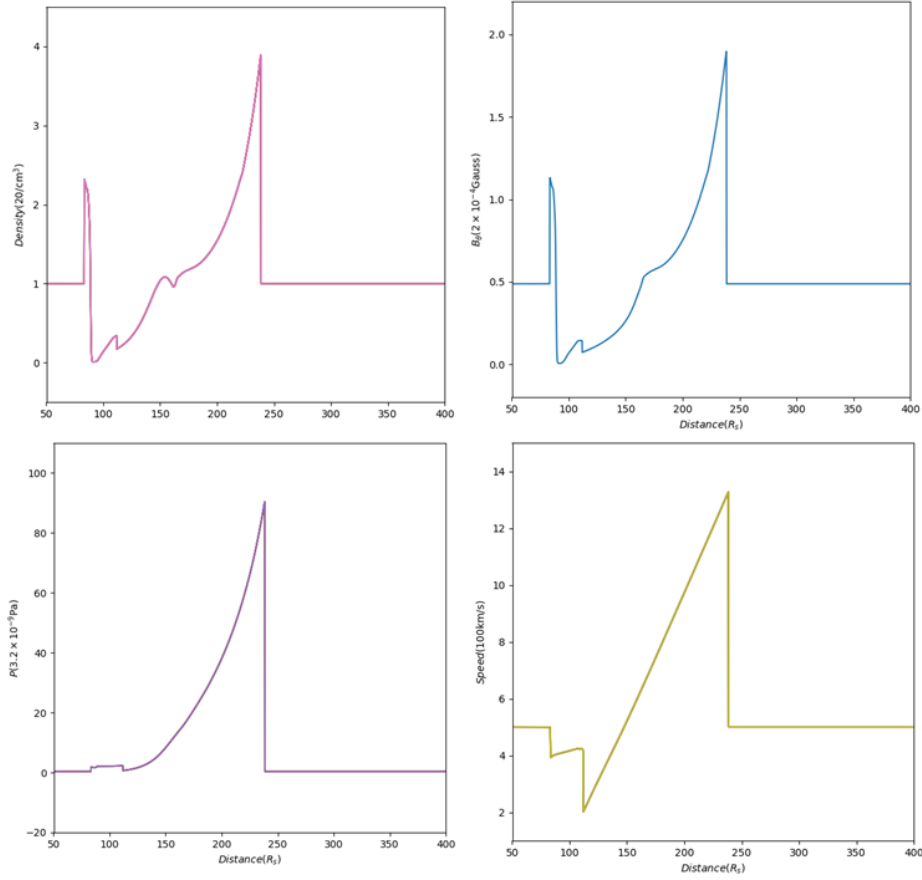
SIMU1

Figure 6: **SIMU1**, 1D: The simulation result of one-dimensional "ICME". The plot gives the spatial distribution of plasma density, magnetic field, pressure and velocity 21 hours after the ICME launched. The Y axis is in code unit (which is non-dimensional), the transformation to the SI unit is given in the label. Please note the small peak behind the depletion region, which may result from the back shock.

The one-dimensional work is inspired by the Riley et al. (2016) using the same **PLUTO** code for the 2012 July event. We used a spatial uniform-distributed density profile with constant outward speed "solar wind" as background, and introduce a $\sin^2$ pulse in density with a much higher speed on the boundary as an "extreme ICME". Figure 6 gives the spatial distribution of four quantities 21 hours after the launch, when the shock front just pasted the 1AU ($1AU = 1.5 \times 10^8$km ≈ 214.3R$_s$).

It is a 1.5D simulation precisely where the differential equations will only be integrated in one dimension while vector(velocity and magnetic field) could have values in more than one dimension. The simulation domain is in the radial direction from $50R_s$ to $400R_s$, with a resolution of 10000 cells. The background density is $20M_p$/cm^3 with a speed 500km/s. The temperature is $2 \times 10^5 K$. During the CME the density plus a term of $20\sin^2(\Delta t)M_p$/cm^3 and the temperature increases to $2 \times 10^6 K$. Here the only non-zero magnetic field component is perpendicular to the radial direction,
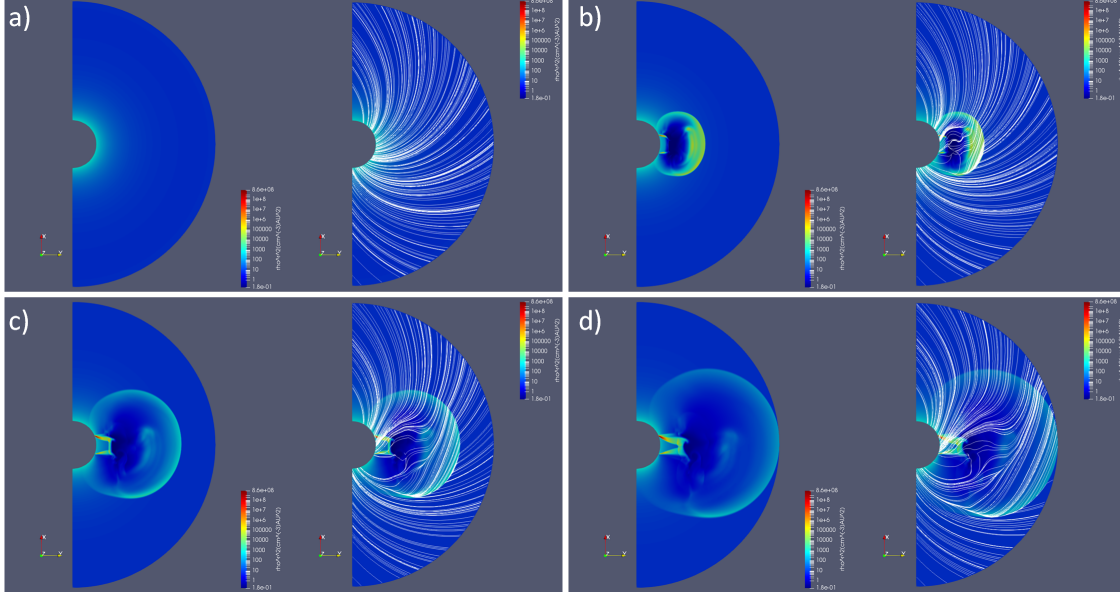
Figure 7: **SIMU2**, $r - \phi$ plane: The density profile and magnetic field lines of a) Stable solar wind just before the launch of ICME, and three states of propagating ICME b) 8 hours, c) 16 hours, d) 24 hours after launch. For a clear illustration, the density is already multiplied by R square and thus have a unit of $\text{cm}^{-3}\text{AU}^2$. As the first two dimensional simulations, all of the magnetic field lines is outward.

where we name as B_θ to show this. The strength is 10^{-4}Gauss.

The CME launched with a speed of 2500km/s and decelerated to nearly 1300km/s at 1AU. It left a trailing depletion region where the density dropped to nearly zero, which will be important for the event in our case study. The vertical magnetic field behaved nearly the same as the density, which is in agreement with the frozen-in theorem.

SIMU2

The first two-dimensional simulation is implemented in the earth rotation frame $(r - \phi)$ plane. We use the rotation frame with an angular velocity of 2.7×10^{-6}rad/s to represent the spin of the Sun. We ran the simulation and reach the steady state, then introduce a similar $\sin^2$ pulse CME in the middle of the simulation region. The steady state of solar wind and three states of propagating ICME are illustrated in figure 7.

The simulation domain covers from $50R_s$ to $300R_s$ in radial direction and a semicircle in $\phi(0$ to $\pi)$, with a resolution of 1000×300. Constant radial velocity and inverse R square density and magnetic field profiles are assigned as the initial condition of the solar wind. The boundary conditions set the plasma density and temperature equal to $60M_p/\text{cm}^3$ and 10^6K on the $r = 50R_s$ for the all time. During the eruption of ICME, the strength of the magnetic field is increased to three times and temperature rise to 2×10^6K. The density inside is set to be

$$\rho(t,\phi) = 60(1 + \sin^2(\pi\frac{t - t_0}{T})\cos(\frac{\pi}{2}\frac{\phi - \phi_0}{\Phi}))$$

$$t_0 < t < t_0 + T, \quad \phi_0 - \Phi < \phi < \phi_0 + \Phi$$

(12)

14

where $T = 1T_U \approx 1.95$hour is the time interval for the whole ICME to go through the boundary $(50R_s)$, and $\Phi = 0.4rad$ is the radius of the CME area. The pressure is proportional to density via

$$p = \frac{T\rho k_B}{\mu m_u} \tag{13}$$

Here M_u is the unit atom mass and μ is the mean molecular weight.

After the solar wind reached its steady state, the pattern of the Parker Spiral of the magnetic field is clearly visible. The plasma flow also follows a nearly identical route travelling outward. While starting with an inverse R square density profile, the gradient in the radial direction of density (as well as temperature) is gentler and behaves like inverse R function when the stable state is reached(a comparison is given in figure 8).
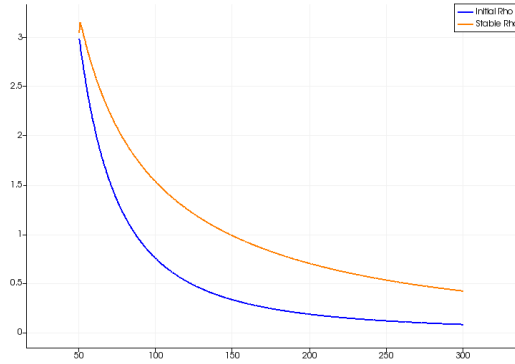
Figure 8: **SIMU2**, $r - \phi$ plane: The comparison of initial and stable density profiles. The Y axis is in code unit.

The initial speed of the ICME is 3000km/s, and it dropped to 1500km/s when arrived at 1AU. The shape of the ICME did not change much during the propagation and expanded both in radial and azimuthal directions. While the CME is a "hydrodynamics object" it still altered the magnetic field structure of solar wind significantly. The magnetic field lines were pushed towards the front surface of the ICME, leaving a depletion region with lower magnetic strength. It is worth to notice that a high-density area appeared behind the shock and have two foot linked to the inner boundary (see c and d in figure 7), which may come from the result of the reverse shock. A similar pattern also occurs in the one-dimensional simulation (see figure 6).

3.2 The Impact of Heliospheric Current Sheet

In the following two simulations, we examined the influence of Heliospheric Current Sheet, or say, the polarity of the Solar magnetic field on the propagation of solar wind and ICMEs.

SIMU3

First, we introduce the polarity in the plane $(r - \theta)$ vertical to earth rotation plane. The resolution remains at 1000×300. The most of the initial condition is the same as the previous simulation except the magnetic field in the north "hemisphere" is outward while in south "hemisphere" inward. The CME will generate on the boundary of the two magnetic fields with opposite
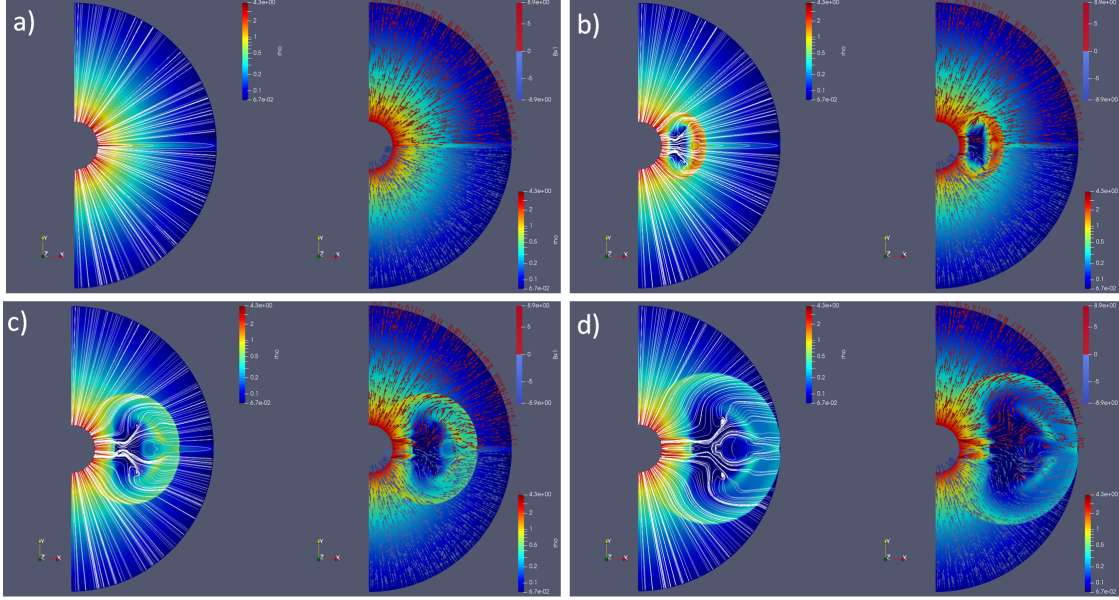
Figure 9: **SIMU3**, $r-\theta$ plane: The density profile and magnetic field lines, and direction of magnetic field of a) Stable solar wind just before the launch of ICME, and three states of propagating ICME b) 8 hours, c) 16 hours, d) 24 hours after launch. The outward and inward magnetic lines is represented by red and blue arrows respectively.
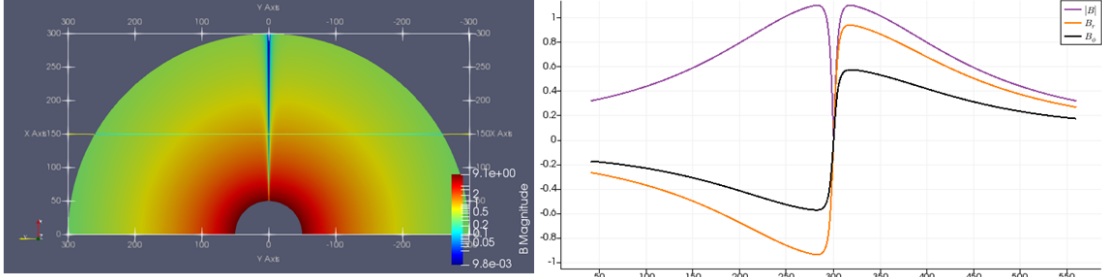

Figure 10: **SIMU3**, $r - \theta$ plane: Left panel: The illustration of Magnetic strength over the simulation domain of stable state. Right panel: The plot of $|B|$, B_r, B_ϕ over the line shows in the left panel. A strong symmetry could be seen. The y axis is in code unit.

directions. During the eruption of ICME, only strength of the magnetic field was increased while the direction was left unchanged. The result is given in figure 9.

When the stable state was reached, a layer with a higher density and low magnetic field strength appeared on the equator, which could be the Heliospheric Current Sheet. Some reconnection happened as a result of the weaker magnetic field in the outer simulation domain. The patterns of magnetic strength, B_r and B_ϕ are illustrated in figure 10. Please notice the symmetry of the field

16

components across the equator.

The deceleration of the ICME underwent in this case is a little weaker than the previous one in the $r - \phi$ plane, which gives the ICME a higher speed nearly 1600km/s when it arrived at 1AU. The distortion of the magnetic field, however, is totally different in this case. A clear reconnection zone is visible behind the shock and is one of the reasons for the enhanced density depletion and the similar high-density region near to the inner boundary (those patterns could be seen in the d) clearly in the figure 9). It is also worth to notice that two turbulent regions appeared during the propagation of the ICME on the two sides of the equator.
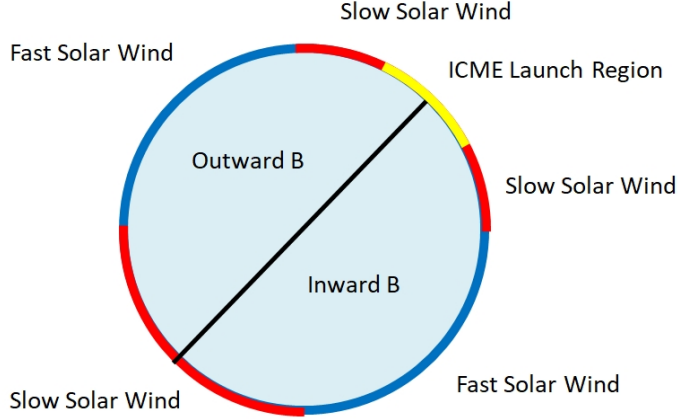
Figure 11: **SIMU4**, $r - \phi$ plane: The boundary condition we used as the equator slide of 5.

SIMU4

In the second simulation about the HCS, we include the fast and slow solar wind regions in the earth rotation plane. The boundary condition is assigned as an equator slide of that shows in figure 5. It is also illustrated more explicitly in figure 11.

This simulation covers a region from $50R_s$ to $250R_s$ and whole azimuthal plane, with a resolution of 400×360. The parameters we used in the simulation are from Odstrcil and Pizzo (1999). The fast solar wind launches in the angular interval $[-0.4, 0.4]$, $[\pi - 0.4, \pi + 0.4]$ with a speed of 600km/s and a density of $30M_p/\text{cm}^3$, with a magnetic field strength twice that in the slow solar wind. The slow solar wind launches in the rest boundary with a speed of 300km/s and a density of $120M_p/\text{cm}^3$. The magnetic field on the semicircle $[-\pi, \pi]$ is outward and inward in the other semicircle.

The result spatial density, magnetic field lines, radial speed and magnetic strength of stable state are shown in figure 12. The heliospheric current sheets were warped with the Parker Spiral and had a higher density compared to the ambient slow solar wind. The stream interaction regions (SIRs) could be seen at the boundary of the fast and slow solar wind, where the density of magnetic lines was higher/lower. Both kind of solar winds accelerated by about 100km/s during the propagation in the simulation domain.

The ICME launched around $\phi = \pi/2$, or say, the top of the inner boundary. While the front shape was not so different from the previous simulation, the inner structure was changed
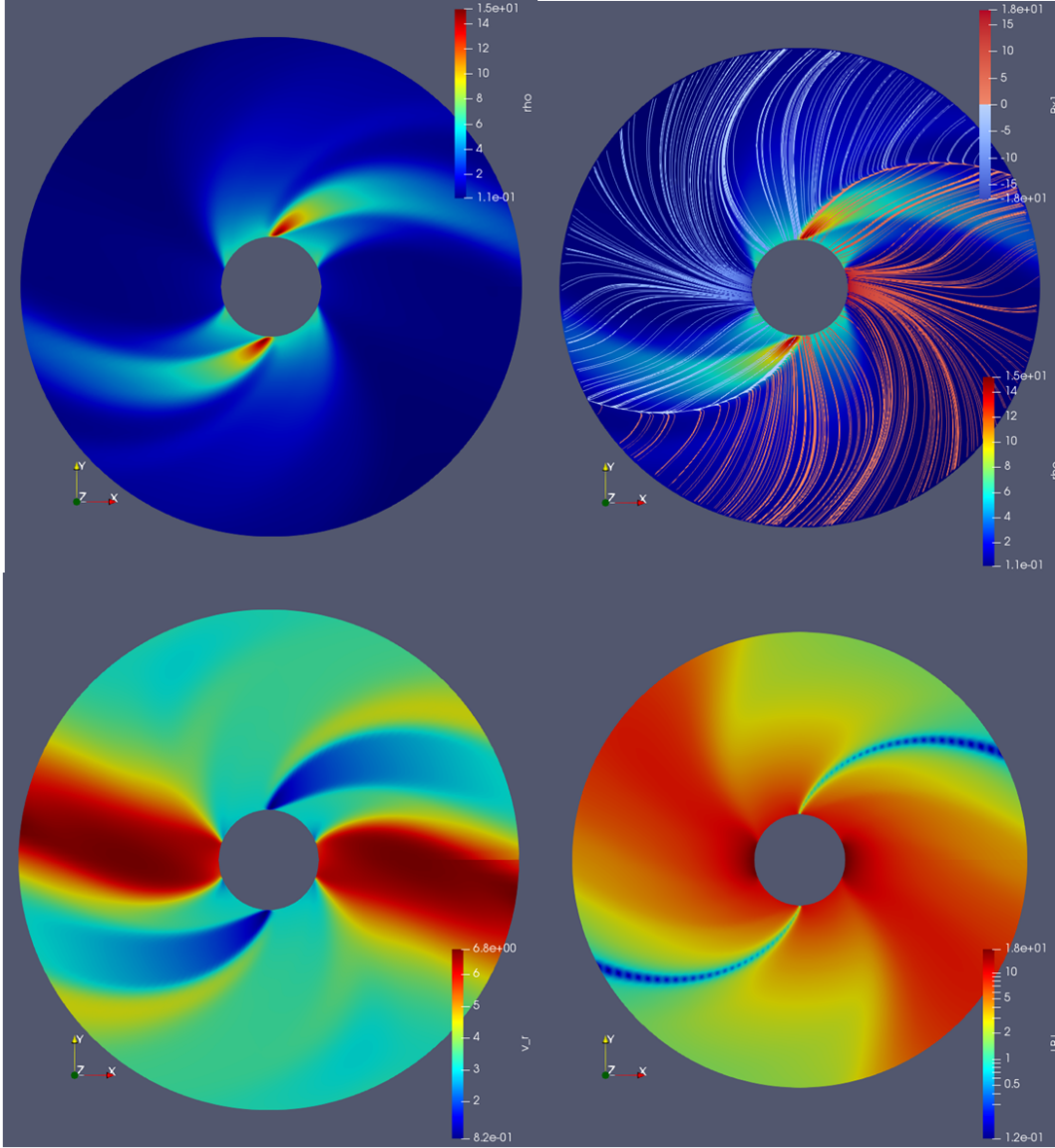
Figure 12: **SIMU4**, $r - \phi$ plane: The density, magnetic field lines and direction (outward red, inward blue), radial velocity, the magnetic strength of the steady solar wind.

significantly. The density depletion was gentler, and the speed of it decreased quicker (from initial 3000km/s to 1300km/s at 1AU) because of the denser current sheet. As shown in the graph, the ICME was trying to push the current sheet and carried it on its way. The original magnetic field was heavily perturbed and recovered slower from the impact of the ICME. Also, the propagation of ICME in the current sheet direction was suppressed because of the higher density.
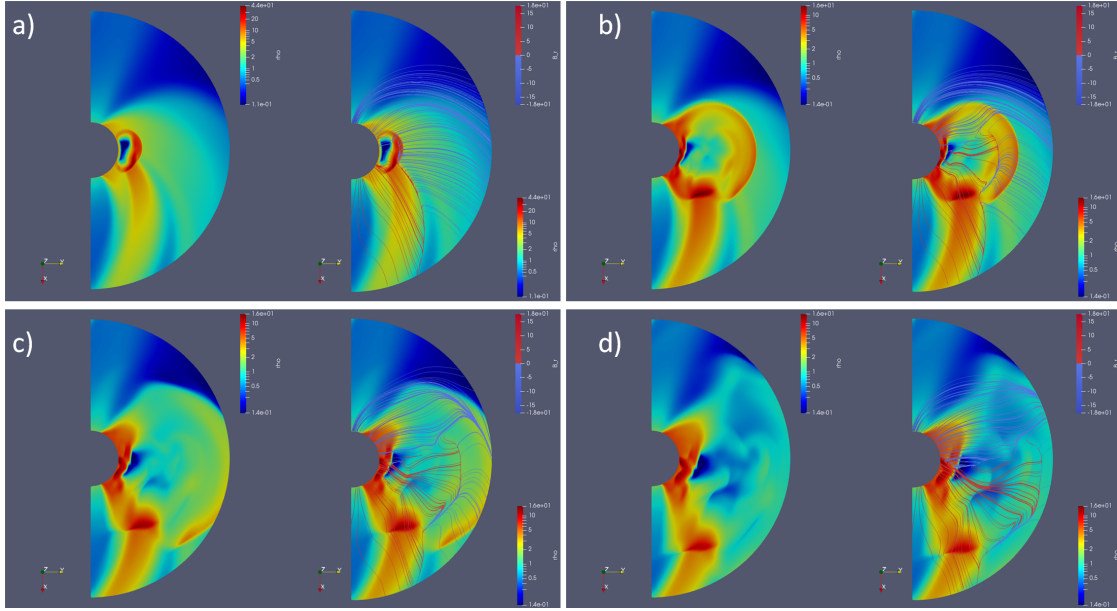
Figure 13: **SIMU4**, $r - \phi$ plane: Density and magnetic field of ICME a) 4 hours, b) 14 hours, c) 24 hours, d) 34 hours after launch. The current sheet was being pushed by the ICME.

As a conclusion, the impact of the HCS on the ICMEs is limited. The most influence it has is on the magnetic field, which is also the incomplete part in our simulations due to the lack of magnetic field structure of the implemented ICMEs. The reader could refer to the paper of Smith (2001) and Hu (1998) on Heliospheric Current Sheet for more information. They discuss how the HCS may not be able to penetrate ICMEs because the CMEs have their unique magnetic topology.

3.3 Three Dimensional Simulation

In this section, we examined the performance of the **PLUTO** in the three-dimensional simulation.

SIMU5

The boundary condition we used, as mentioned above, is shown in figure 5. A clearer illustration is given in figure 14. It assumes a time in the solar minimum period when the streamer belt and corona holes are distinguishable on the surface of the Sun, with the transitions regions as the boundaries between them.

For a more realistic transition region, we refer the idea of Harris Current Sheet where a tanh function is used for the jump between two constant values condition. In this assumption, the velocity of solar wind is represented by

$$v(\theta) = v_f - \frac{\Delta v}{\pi}(-\tanh(\frac{\theta - \theta_1}{\Delta\theta}) + \tanh(\frac{\theta - \theta_2}{\Delta\theta})) \tag{14}$$

where v_f is the velocity of fast solar wind, $\Delta v = v_f - v_s$ is the difference between the velocity of the fast and slow solar wind. θ_1, θ_2 are the coordinates of two transition region, and $\Delta\theta$ is the typical
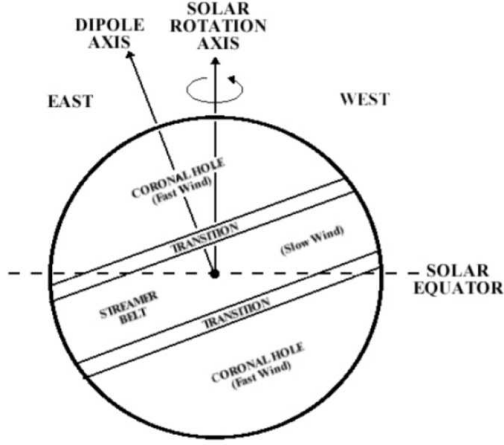
19

Figure 14: **SIMU5**, 3D: The source surface at $50R_s$ as the inner boundary for the 3D simulation. Please be aware that the polarity of magnetic fields differs for two hemispheres, so there are four layers in total.

width of them. Please notice all polar angles θ here are referred to the axis of dipole which is tiled (see figure 14). The densities and velocity parameter we use is from Odstrcil and Pizzo (1999).

The expression above imitate the profiles below:

$$v(\theta) = \left\{ \begin{array}{ll} v_f & \theta < \theta_1 \\ v_s & \theta_1 < \theta < \theta_2 \\ v_f & \theta > \theta_2 \end{array} \right. \tag{15}$$

The expression of the magnetic field follows a similar idea as well and gives

$$\mathbf{B}(\theta) = \frac{2\mathbf{B}_0}{\pi}(\frac{1}{2}\tanh\frac{(\theta - \theta_1)}{\Delta\theta} + \tanh\frac{\theta}{\Delta\Theta} + \frac{1}{2}\tanh\frac{(\theta - \theta_2)}{\Delta\theta}) \tag{16}$$

Here $\mathbf{B}_0$ is the magnetic field strength. It leads to the profile of

$$\mathbf{B}(\theta) = \left\{ \begin{array}{ll} 2\mathbf{B}_0 & \theta < \theta_1 \\ \mathbf{B}_0 & \theta_1 < \theta < \frac{\pi}{2} \\ -\mathbf{B}_0 & \frac{\pi}{2} < \theta < \theta_2 \\ -2\mathbf{B}_0 & \theta > \theta_2 \end{array} \right. \tag{17}$$

We assume the magnetic field strength in the fast solar wind region is twice of that in the slow solar wind.

The simulation covers a domain that consists of $200 \times 90 \times 180$ cells from $50R_s$ to $250R_s$, from $\pi/6$ to $5\pi/6$ in polar angle and the whole azimuthal plane. The resolution in every dimension is decreased for better computational performance. The coordinates we use is the HEE(Heliocentric Earth ecliptic). The steady solar wind is illustrated in figure 15. The main pattern is quite similar to the two-dimensional simulation above, especially on the equator plane. The solar wind kept accelerating in the inner heliosphere and reached its final velocity of around $140R_s$. The density
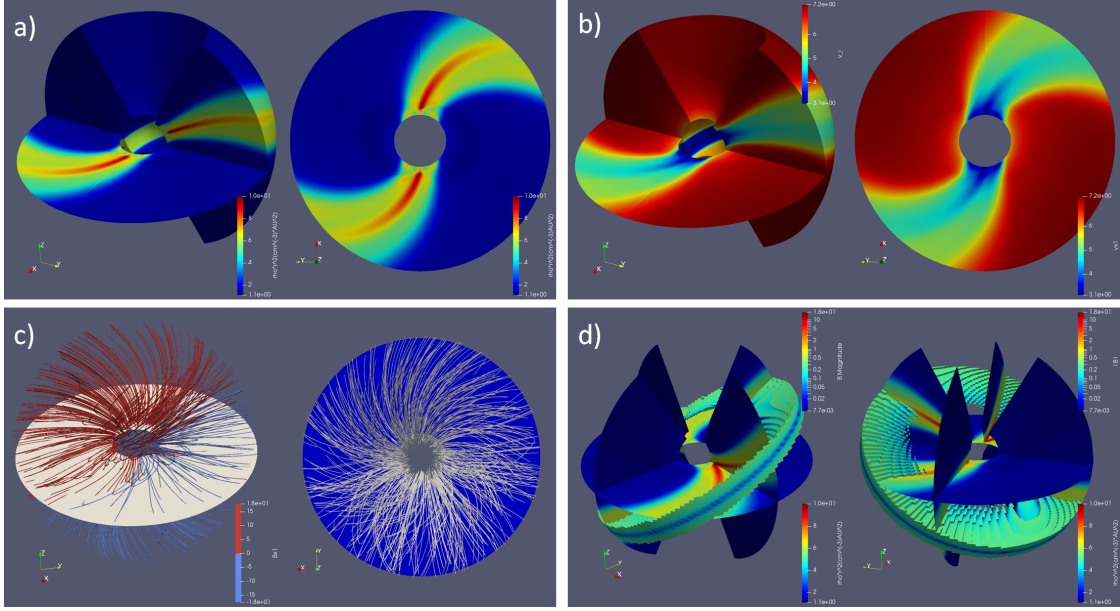
20

Figure 15: **SIMU5**, 3D: The spatial distribution of a) density (multiplied by R square) b)velocity c)magnetic field lines and d)Heliospheric Current Sheet for the stable state. The HCS is extracted by setting a threshold on the strength of the magnetic field.

dropped quickly in the radial direction and followed an inverse R square profile after the maximum velocity of solar wind is reached. This result is consistent with the flow conservation relation which has a formulation of

$$\rho v r^2 = \text{constant} \tag{18}$$

The Heliospheric Current Sheet here has the shape of a nearly standard circle because our simulation just covered the inner heliosphere where the Parker Spiral is not so notable to warp it.

The result of ICMEs simulation in this background is given in figure 16. Here we set the quantities in the ICME as

$$\rho(t, \theta, \phi) = \rho_{sw}(1 + 2\sin^2(\pi\frac{t - t_0}{T})\cos(\frac{\pi}{2}\frac{\Delta\psi}{\Psi})) \tag{19}$$
$$t_0 < t < t_0 + T, \quad \Delta\psi < \Psi$$

Where

$$\Delta\psi(\theta, \phi) = \sqrt{(\theta - \theta_0)^2 + (\phi - \phi_0)^2} \tag{20}$$

and $\Psi = 0.3$rad is the radius of ICME when it went through the inner boundary.

Generally speaking, the 3D ICME propagation in the heliosphere is similar to the 2D version. The ICME, which launched with a speed of 3000km/s, decelerated to nearly 1500km/s at 1AU. A high-density region was formed when it crossed the HCS. It also leads to the deflection of the fastest propagation direction of ICMEs, as mentioned in Hu (1998). The fast solar wind, as a medium with lower density and faster speed, causes less deceleration of the shock. As a result, the propagation
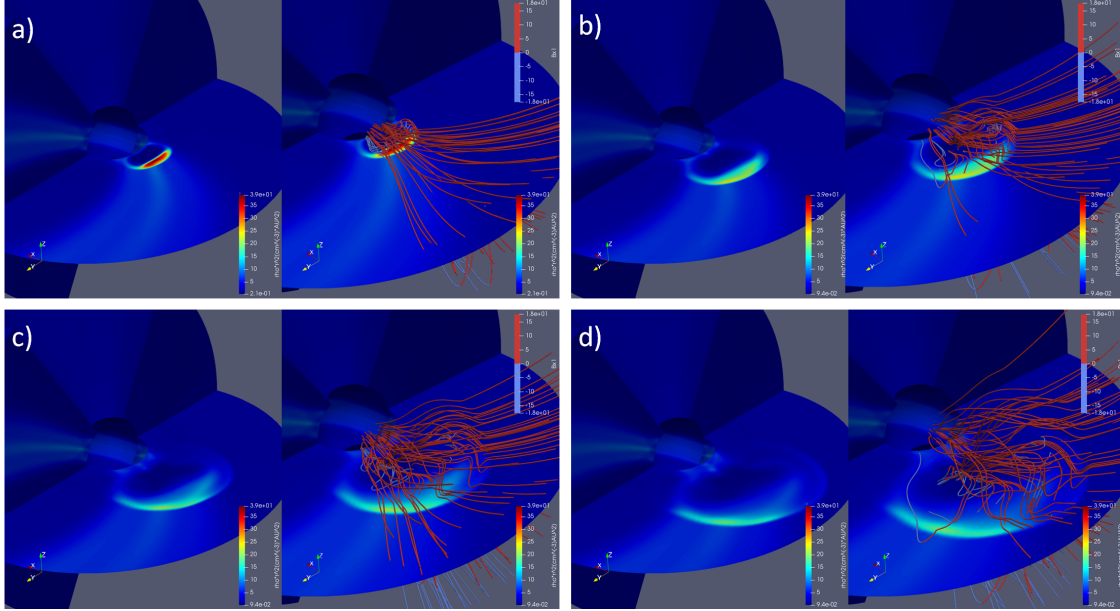
21

Figure 16: **SIMU5**, 3D: The density and magnetic field lines for the ICME a) 4 hours b)8 hours c)12 hours d) 16 hours after the launch. It arrives 1AU in around 17 hours. The magnetic lines of the ambient solar wind are pushed away by the shock of the ICME.

of ICMEs in the fast solar wind will be quicker than that in the slow solar wind, and makes the fast propagation direction changed in its way (see figure 17).

It is worth to mention the impact of adiabatic index γ on the simulation result. If the solar wind consists of proton and electron ideally, the γ will be very close to the monatomic value of 5/3. However, a smaller adiabatic index could be used to approximate the kinetic phenomena far below the MHD scale and heating process we mentioned in the introduction. A smaller γ provides a gentler gradient of temperature in the radial direction. See figure 18. The deviation from the pure adiabatic expansion of the solar wind is often referred to as "solar wind heating" problem, which results in the unexpected high temperature of electron and other particles in the solar wind. Much theoretical work has been done to investigate this phenomenon, include theories based on cyclotron resonance of ions and electrons (Isenberg and Hollweg, 1983; Cranmer, 2014). Some recent research indicates the heating is a result of Landau damping of turbulence in the space and provides evidence from observation in the energy transfer between the turbulent electromagnetic field and electrons near the Earth(Chen et al., 2019).

SIMU6

As the final part of our work, we did the data-driven simulation for testing the compatibility of the **PLUTO** code. As we mentioned before, we read the data of **ENLIL** on the $30R_s$ as boundary conditions instead of assigning them by hand. The **ENLIL** links to the MAS and WSA model using empirically derived boundary condition. And the latter two models do the simulation back to the surface of the Sun, by using the (filtered) magnetogram from the Kitt Peak Observatory. These models have been providing decent space weather forecast for a decade, and they are also available
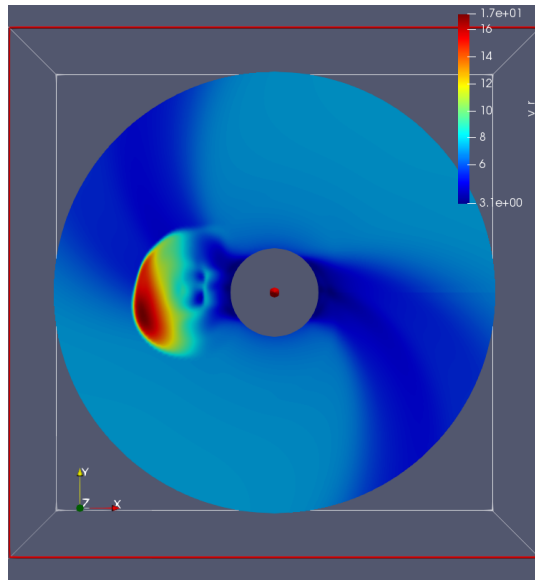
Figure 17: **SIMU5**, 3D: The radial velocity profile 14 hours after the launch. The original ICME is symmetry around the X axis, while the fastest propagation direction is deflected off the X axis, toward the fast solar wind region.
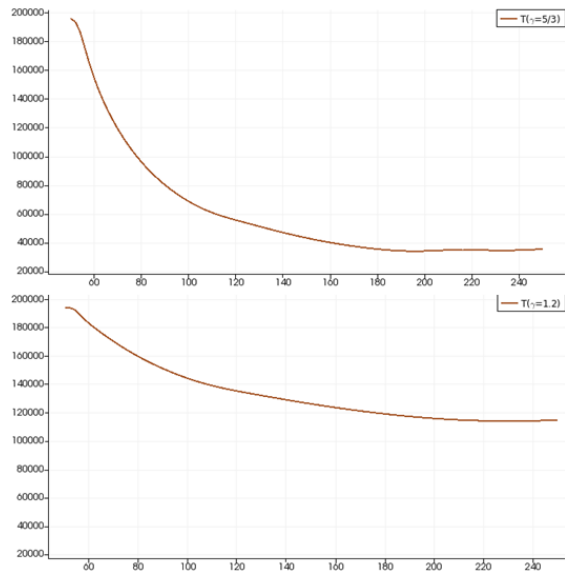

Figure 18: The comparison of temperature profile over the radial direction. The temperature drops much more slowly when $\gamma = 1.2$, compare to that in $\gamma = 5/3$

to the public to request a run for solar wind in the past years, based on the archived data.

The data our simulation based on is between 2012 July 10th to 2012 July 28th. The parameters we use for the empirically derived boundary condition of **ENLIL** gives as below:

$$\begin{aligned}
\rho_{in} &= 150 M_p/\text{cm}^3 \\
v_{ssw} &= 250 \text{km/s} \\
v_{fsw} &= 650 \text{km/s} \\
T &= 6 \times 10^5 K \\
B &= 150 \text{nT}
\end{aligned} \tag{21}$$

Those quantities are all assigned on the inner boundary of $30R_s$. The ρ_{in} is the density, and the T is the mean temperature. The B specified the magnetic field strength in the fast solar wind region.

The **ENLIL** gives the values of quantities we interested on the boundary as an ASCII text list every 6 hours. The raw angular resolution of **ENLIL** is 180×360 (in θ and ϕ direction, respectively), but the data is also available in different resolution. Here we used the resolution of 90×180 same as our simulation domain for a higher computational speed.

Spline interpolation is implemented after reading the raw data files to deal with the rather low time resolution (only four files for a whole day). For every boundary point at every time step, we input four values from the four nearest time files and interpolate to get the approximate value on the current time. This process is pretty computational-consuming and leads to a drop in simulation performance.

We use a simulation domain of $192 \times 90 \times 180$ cells for a space of $[30R_s, 300R_s] \times [\pi/6, 5\pi/6] \times [0, 2\pi]$. The initial condition is not important because the final stable state depends on the plasma flow from the inner boundary. It takes nearly 90 unit of code time (about one week in real time) for the system to reach its steady state, and it is shown in figure 19.

The pattern of real solar wind is much more complicated, with multiple fast and slow flow regions seen in the domain. Between them the stream interaction regions appear: the fast solar wind compressed the preceding slow solar wind, and left a gap between it and trailing slow solar wind. It leads to density enhanced and depleted areas, which could be seen clearly from the two upper panels of figure 19. Except the two extreme fast stream with a velocity of nearly 900km/s, the fast solar wind has a typical velocity of 600km/s and a density several proton mass per cube centimeter when it arrives 1AU, while the slow solar wind has a speed of around 300km/s and a density of $10 - 20 M_p/\text{cm}^3$ at that position.

Given the solar wind launch pattern, the shape of the heliospheric current sheet is also complicated, compared to the previous simulations. It is illustrated roughly in figure 20. The magnetic field of a stable state follows the Parker Spiral, and its spiral angle varies with the latitude. The angle reached its maximum near the equator, and it is in agreement with the analytical result (Meyer-Vernet, 2007). The angle is more than 45 degree at 1AU (defined as $\Theta \equiv \arctan(|B_\phi/B_r|)$) and the strength of magnetic field is in the order of 10nT at 1AU. The strength is higher in the fast solar wind.

For a clean presentation, we just include the solar wind par here for the data-driven simulation. please refer to the next section of the case study for the simulation of ICME in this realistic ambient solar wind.
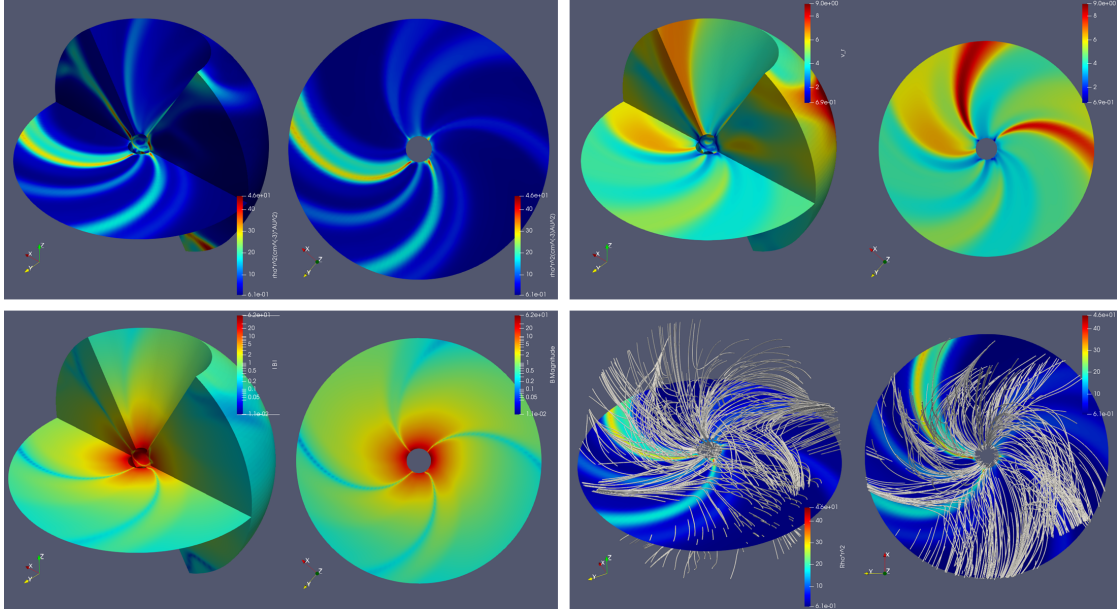
24

Figure 19: **SIMU6**, 3D: The simulation result of the data-driven solar wind. Left upper panel: the distribution of density (multiplied by R square). Right upper panel: the distribution of radial velocity. Left lower panel: The strength of the magnetic field. Right lower panel: The magnetic field lines. The spiral angle varies with the latitude.
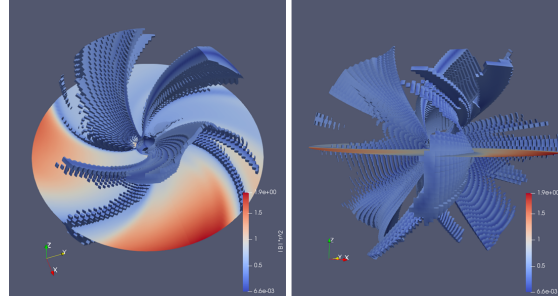

Figure 20: **SIMU6**, 3D: The warped heliospheric current sheet. It is illustrated by setting a threshold on magnetic field strength. It has a trend of "the ballerina skirt".

4 Case Study: the 2012 July Extreme CME Event

The extreme CME is a particular interest of space physics research for its strength and potential damage to modern society. On 23rd July 2012, a Carrington-Class CME was recorded by twin satellites Stereo-A, B and SOHO (Solar and Heliosphere Observatory). In this section, we investigate this CME event using the simulation tools we established above.

4.1 Observation

The positions of the three satellites mentioned at that time of the CME eruption are plotted in the figure 21 (SOHO is near the position of the earth). This CME was launched in the solar active
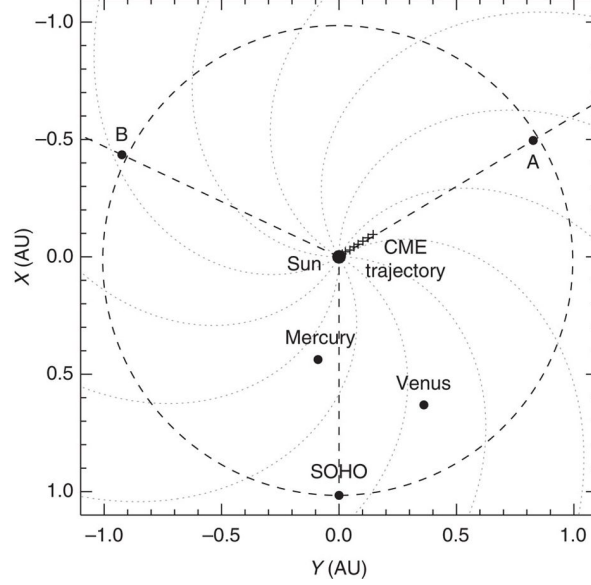

Figure 21: The illustration of position for the three satellites and inner heliosphere planets. The Stereo-A, B were 121.3 degrees west and 114.8 degrees east of the earth and distances of 0.96AU and 1.02AU from the Sun. The interplanetary magnetic field is represented by the dotted lines. Taken from Liu et al. (2014).

region 1520 at 02:27 UT on the 23rd and started with two successive prominence eruptions (Liu et al., 2014). The two CMEs they generated merged close to the sun due to CME-CME interaction, and a shock was developed during the same period. The coronagraphs of the eruption were taken by COR1 and COR2 of Stereo-A, B, and two of these images are given in figure 22.

The triangulation measurement technique (Liu et al., 2010) was used to determine the kinetic properties of this event. The CME is measured having an initial speed of 2500 ± 500km/s and a propagating direction angle of about 10 degrees off the Sun-StereoA lines. The propagation direction underwent a transition towards the Sun-StereoA lines when the CME reached about 6-11 R_s. It may result from the CME-CME interaction we mentioned above (Liu et al., 2019). The velocity of the (I)CME dropped to about 2700km/s from its peak of 3050km/s when it goes through the surface of $30R_s$.

This extreme event is measured in situ by the Stereo-A, which is right in front of the propagation direction. The recording data of proton number density n_p, bulk velocity v_p, proton temperature T_p, strength and components of the magnetic field are given in figure 23. The data of proton density and temperature was largely missed during this event because they exceeded the normal detector range. Here the density is calculated from the density of electrons with an energy higher than 45eV (multiplied by 5). The temperature profile is from 1D Maxwellian fit.
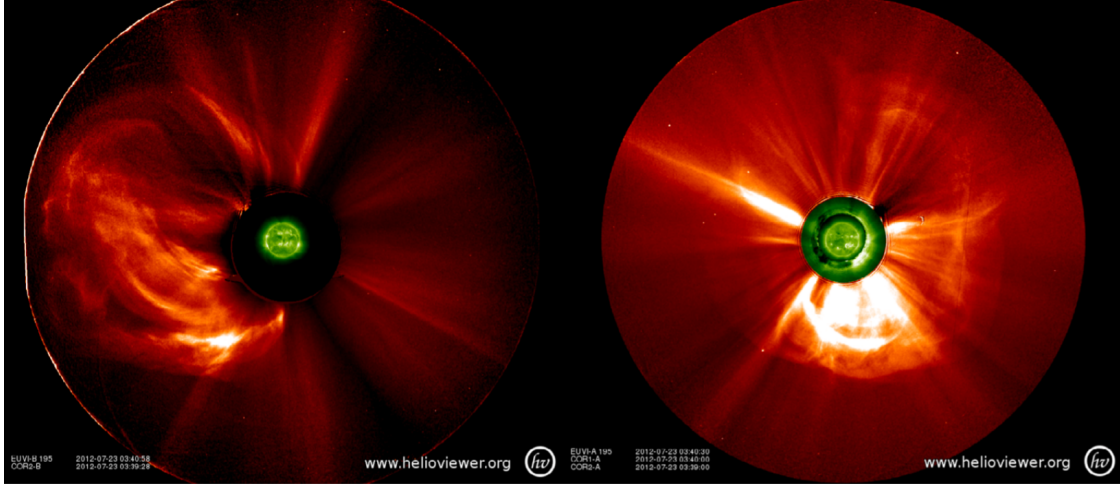
Figure 22: Images of the CME in progress. They were taken by Stereo-B (left) and Stereo-A at about 03:40 UT on 23rd July. A shock already appeared and could be seen easily in the left picture. The graph in the centre of the two picture is a solar disk $195\mathring{A}$ image taken by STEREO SECCHI EUVI(Extreme Ultraviolet Imager) instruments. Taken from Baker et al. (2013).

The CME arrived at the position of Stereo-A 18.6 hours after it launched from the corona, with an average traveling speed around 2150km/s (Riley et al., 2016). The estimated shock speed observed by Stereo-A is about 2250km/s. Considering its initial speed, the CME only suffered a marginal slowdown in its way to 1AU. Several hypothesis have been put forward to explaining this (Liu et al., 2017). And among this there is a popular one considering the idea that a preceding CME helps to clean the path of this extreme CME. The first CME launched in the same region as the second one, and followed a similar route in the heliosphere. It left a density depletion region trailing it where the second went through, leading to a slower deceleration of the second one because of the weaker solar wind drag. In the simulation part, we examined this idea and studied how the time gap between the two CMEs affects the result.

4.2   Simulation

The final part of the section 3 provides the simulation of solar wind driven by **ENLIL** data. Here we use it as our background. After the solar wind reaches its stable state on July 18th, we keep inputting the boundary data from **ENLIL** and extend it to 28th. To synthesize the in situ measurement of Stereo-A in our simulation, we insert a probe in our calculation domain according to the position information of stereo-A from **HORIZONS** System[1]. The system provides high accuracy position of the satellite during the interested period, and spline interpolation is used to calculate the exact position at the code time during the simulation.

Please notice most of the parameters we used in our simulation are referred to the paper of Liu et al. (2014). The first CME was launched (more precisely, when it went through the surface

---

[1]HORIZONS is an ephemeris computation service produced by the Solar System Dynamics Group of the Jet Propulsion Laboratory, USA.
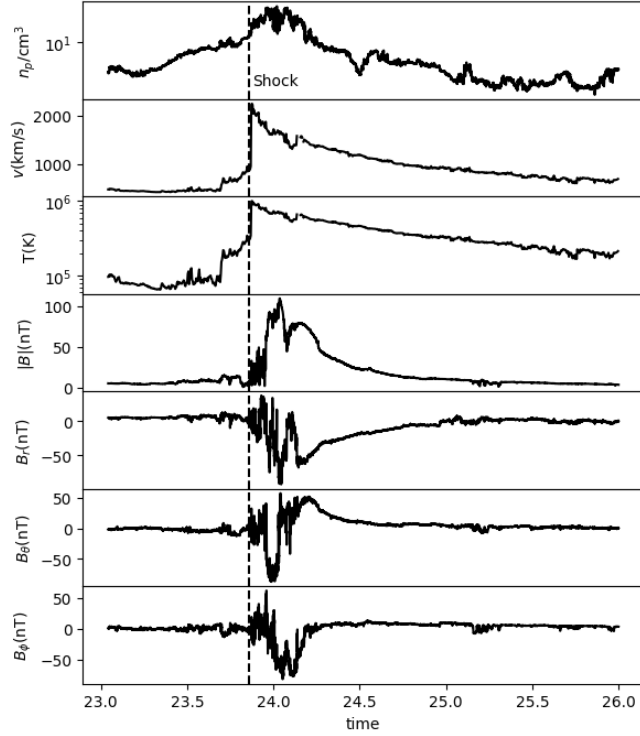
Figure 23: The in situ measurement of the ICME quantities (from the top to bottom: proton number density, bulk velocity, proton temperature, the strength of the magnetic field and its three components. The components are given in HEE spherical coordinate. The vertical dashed lines show the arrival time of the ICME shock.

of $30R_s$) at 05:30 UT on 19th July with a medium density and magnetic field, and a velocity of 1600km/s. The second CME was launched at 04:30 UT on 23rd with a pretty high density and magnetic field. The initial speed of it was 2800km/s.

We first examined the performance of MHD simulation of this event, but the result was quite unsatisfying. The solar wind recovers quickly after the first CME and left little effect on the second one, the simulation also gave a messy magnetic field result, compared to the real measurement. The figure 24 provides a typical MHD simulation result.

The reason of the bad simulation is the lack of the magnetic field structures in our CMEs. As we mentioned above, the standard flux rope structure requires a simulation domain back to the surface of the Sun to include the corona region, and it is rather hard to implement it in our model. To avoid this problem and inspired by the solution of the **ENLIL** and **EUHFORIA**, we tried to simulate this event with hydrodynamics module. At the cost of magnetic field information, the HD simulation gave a more realistic result consistent with the data in density and velocity.

The density profiles of the HD simulation are illustrated in fig 25. The density depletion region trailing the first CME lasted for a quite long time, which the second one went through. The CME underwent a shape distortion because it propagated faster in this region, where it even experienced
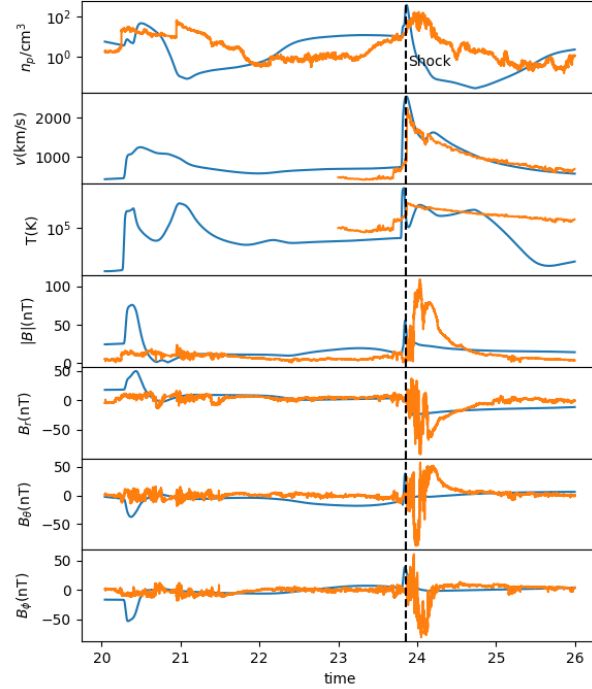
28

Figure 24: The MHD simulation result given in synthetic plot of Stereo-A. The orange lines show the real measurement as a comparison. Please notice the quick raise in density after the first CME. The variance of the magnetic field is also too small with a peak of only 50nT.

a small acceleration. This could be seen in figure 26 illustrating the velocity change before and after the CME travelled into the depletion area. The synthetic Stereo-A measurement plots compared to the real one are given in figure 27. There is a pretty good fit in profiles of density and velocity while disagreement occurs in the temperature measurement. It may result from the absence of unideal heating mechanism like turbulence in our system. It is quite clear the preceding CME could help the latter one propagate faster from the above simulation, and this is the reason, at least one of the reasons account for the extreme CME event on 2012 July 23rd. In the next stage, we examined the effect of the time gap between two CMEs would have on this enhancement. We varied the launch time of the second main CME from 18:20 UT 20th to 14:40 UT 25th while keeping everything else unchanged, then we extracted the peak shock velocity and proton density of the second CME to plot the figure 28 The effect of enhancement lasts for around two days, then it decays and finally meets the other lines without the preceding CME. When the effect on its maximum, the shock velocity of the second CME would increase by approximately 1000km/s. Another interesting result is that there is not too much difference in peak density between the cases of presence and absence
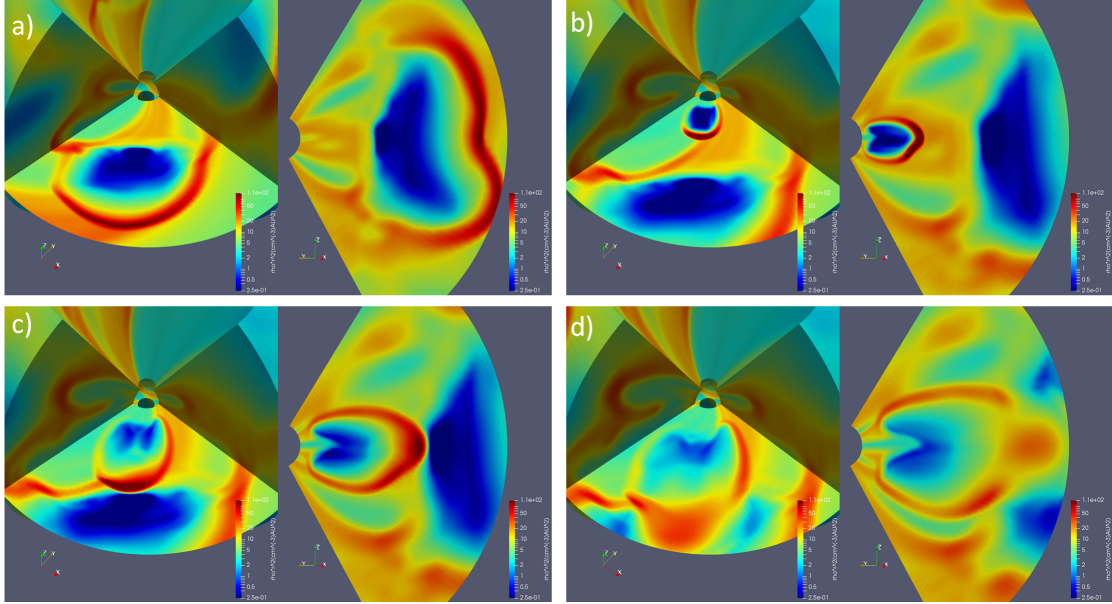
Figure 25: The density profile (multiplied by R square) are given in times points when a) 64 hours b) 100 hours after the first CME launched, and c) 12 hours d) 24 hours after the second CME launched. The second CME distorted after it propagated into density depletion region.
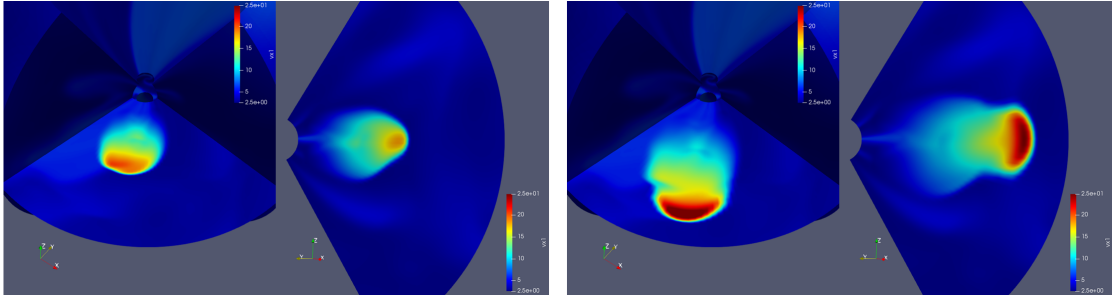

Figure 26: The velocity illustration before and after the CME entered the depletion area. It is clear that its propagation speed toward this area was much higher.

of the preceding CME, and it is higher in the latter situation. It may come from the "stretch" of the CME front when it travels into a density depletion region (see (d) in figure 25).

As a belief conclusion, the successive eruption of CMEs have the potential to create a fiercer event if they are close enough in time and space, and it is mainly due to the density depletion region behind the preceding CMEs. The CMEs ahead may also affect the interplanetary magnetic environment, which could not be shown in our HD simulation. For instance, It is believed that the CME ahead can stretch the interplanetary magnetic field along the radial direction, reduces the magnetic tension force applied on the following CME(Liu et al., 2014).
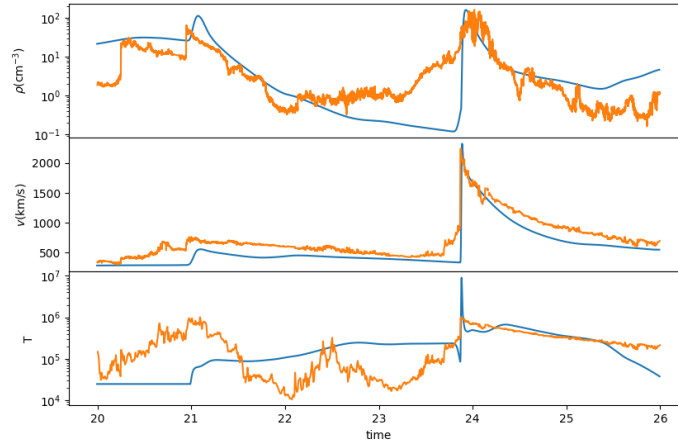
Figure 27: The result of HD simulation compared to the real measurement. The density and velocity profiles are largely consistent with the data, though the simulation can not reveal the temperature change correctly during this period.
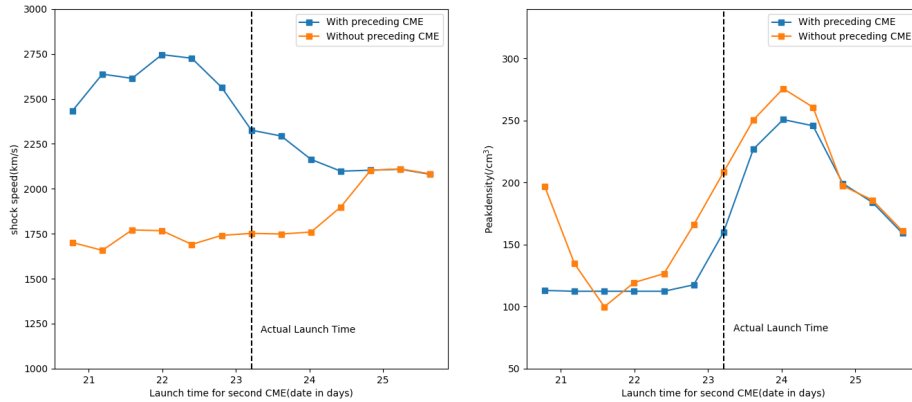

Figure 28: The peak shock velocity and number density as functions of launch time of the second CME. The enhancement effect from the first CME remains for several days before finally fades. It does not affect heavily on the peak density, whose fluctuation mainly depends on the ambient solar wind.

5   Discussion and Conclusion

In this study, we simulated the solar wind and ICME propagation in the inner heliosphere using the code of **PLUTO**. We started at the simplest case in one dimension and then moved to

more complicated and realistic multi-dimensional simulations. The result we presented here could successfully reproduce the main structure of solar wind, and provide a decent picture of propagating ICMEs.

We also examine the compatibility of the code with the data-driven simulation, aiming for space weather forecasting. It is shown that **PLUTO** could receive input boundary condition from data smoothly, and produce results similar to **ENLIL**. Based on the data-driven solar wind background, we studied the 2012 July 23rd ICME event mainly using the HD module. We introduced two successive CME and investigated the effect of the preceding one on the latter one, which is believed to be one reason for why the 2012 event was so extreme. Though lacking in magnetic information, the simulation provides a rather good imitation with the in situ measurement in proton density and velocity, proved the enhancement effect via density depletion region trailing the first CME.

As a heliosphere simulation project, we do not implement any magnetic structure in our CMEs. The results, however, are satisfying enough and achieve our goals. The introduction of a corona region and correct flux rope models for CMEs could increase the quality of simulation significantly at the cost of calculating speed, and for this reader could refer to paper we mentioned in the Introduction section. However, many works remain to be done before these more accurate and "expensive" models could be used in the real-time space weather forecast.

References

Baker, D.N., Li, X., Pulkkinen, A., Ngwira, C.M., Mays, M.L., Galvin, A.B., Simunac, K.D.C., 2013. A major solar eruptive event in july 2012: Defining extreme space weather scenarios. Space Weather 11, 585–591. doi:10.1002/swe.20097.

Carrington, R.C., 1859. Description of a Singular Appearance seen in the Sun on September 1, 1859. mnras 20, 13–15. doi:10.1093/mnras/20.1.13.

Chen, C.H.K., Klein, K.G., Howes, G.G., 2019. Evidence for electron Landau damping in space plasma turbulence. Nature Communications 10, 740. doi:10.1038/s41467-019-08435-3, arXiv:1902.05785.

Cranmer, S.R., 2014. Ensemble Simulations of Proton Heating in the Solar Wind via Turbulence and Ion Cyclotron Resonance. apjs 213, 16. doi:10.1088/0067-0049/213/1/16, arXiv:1406.0678.

van Driel-Gesztelyi, L., Culhane, J.L., 2009. Magnetic flux emergence, activity, eruptions and?magnetic clouds: Following magnetic field from?the?sun to the heliosphere. Space Science Reviews 144, 351–381. doi:10.1007/s11214-008-9461-x.

Forbes, T.G., Linker, J.A., Chen, J., Cid, C., Kóta, J., Lee, M.A., Mann, G., Mikić, Z., Potgieter, M.S., Schmidt, J.M., 2006. CME Theory and Models. ssr 123, 251–302. doi:10.1007/s11214-006-9019-8.

Gibson, S.E., Low, B.C., 1998. A Time-Dependent Three-Dimensional Magnetohydrodynamic Model of the Coronal Mass Ejection. apj 493, 460–473. doi:10.1086/305107.

Gonzalez, W.D., Joselyn, J.A., Kamide, Y., Kroehl, H.W., Rostoker, G., Tsurutani, B.T., Vasyliunas, V.M., 1994. What is a geomagnetic storm? jgr 99, 5771–5792. doi:10.1029/93JA02867.

van der Holst, B., Sokolov, I.V., Meng, X., Jin, M., W. B. Manchester, I., Tóth, G., Gombosi, T.I., 2014. ALFVén WAVE SOLAR MODEL (AWSoM): CORONAL HEATING. The Astrophysical Journal 782, 81. URL: https://doi.org/10.1088%2F0004-637x%2F782%2F2%2F81, doi:10.1088/0004-637x/782/2/81.

Hu, Y.Q., 1998. Asymmetric propagation of flare-generated shocks in the heliospheric equatorial plane. jgr 103, 14631–14642. doi:10.1029/97JA03527.

Hundhausen, A.J., Burkepile, J.T., St. Cyr, O.C., 1994. Speeds of coronal mass ejections: SMM observations from 1980 and 1984-1989. jgr 99, 6543–6552. doi:10.1029/93JA03586.

Isenberg, P.A., Hollweg, J.V., 1983. On the preferential acceleration and heating of solar wind heavy ions. jgr 88, 3923–3935. doi:10.1029/JA088iA05p03923.

Kahler, S.W., 1992. Solar flares and coronal mass ejections. araa 30, 113–141. doi:10.1146/annurev.aa.30.090192.000553.

Liu, Y., Davies, J.A., Luhmann, J.G., Vourlidas, A., Bale, S.D., Lin, R.P., 2010. Geometric Triangulation of Imaging Observations to Track Coronal Mass Ejections Continuously Out to 1 AU. The Astrophysical Journal 710, L82–L87. doi:10.1088/2041-8205/710/1/L82, arXiv:1001.1352.

Liu, Y.D., Hu, H., Zhu, B., Luhmann, J.G., Vourlidas, A., 2017. Structure, Propagation, and Expansion of a CME-driven Shock in the Heliosphere: A Revisit of the 2012 July 23 Extreme Storm. The Astrophysical Journal 834, 158. doi:10.3847/1538-4357/834/2/158, arXiv:1611.04239.

Liu, Y.D., Luhmann, J.G., Kajdič, P., Kilpua, E.K.J., Lugaz, N., Nitta, N.V., Möstl, C., Lavraud, B., Bale, S.D., Farrugia, C.J., Galvin, A.B., 2014. Observations of an extreme storm in interplanetary space caused by successive coronal mass ejections. Nature Communications 5, 3481. doi:10.1038/ncomms4481, arXiv:1405.6088.

Liu, Y.D., Zhao, X., Hu, H., Vourlidas, A., Zhu, B., 2019. A comparative study of 2017 july and 2012 july complex eruptions: Are solar superstorms "perfect storms" in nature? The Astrophysical Journal Supplement Series 241, 15. URL: https://doi.org/10.3847%2F1538-4365%2Fab0649, doi:10.3847/1538-4365/ab0649.

MacQueen, R.M., Csoeke-Poeckh, A., Hildner, E., House, L., Reynolds, R., Stanger, A., Tepoel, H., Wagner, W., 1980. The High Altitude Observatory coronagraph/polarimeter on the Solar Maximum Mission. solphys 65, 91–107. doi:10.1007/BF00151386.

Manchester, Ward B., I., Vourlidas, A., Tóth, G., Lugaz, N., Roussev, I.I., Sokolov, I.V., Gombosi, T.I., De Zeeuw, D.L., Opher, M., 2008. Three-dimensional MHD Simulation of the 2003 October 28 Coronal Mass Ejection: Comparison with LASCO Coronagraph Observations. apj 684, 1448–1460. doi:10.1086/590231, arXiv:0805.3707.

Manchester, W., Kilpua, E.K.J., Liu, Y.D., Lugaz, N., Riley, P., Török, T., Vršnak, B., 2017. The physical processes of cme/icme evolution. Space Science Reviews 212, 1159–1219. doi:10.1007/s11214-017-0394-0.

Manchester, W., Ridley, A., Gombosi, T., DeZeeuw, D., 2006. Modeling the sun-to-earth propagation of a very fast cme. Advances in Space Research 38, 253 – 262. doi:https://doi.org/10.1016/j.asr.2005.09.044. the Great Historical Geomagnetic Storm of 1859: A Modern Look.

Manchester IV, W.B., Gombosi, T.I., Roussev, I., Ridley, A., De Zeeuw, D.L., Sokolov, I.V., Powell, K.G., Tth, G., 2004. Modeling a space weather event from the sun to the earth: Cme generation and interplanetary propagation. Journal of Geophysical Research: Space Physics 109. doi:10.1029/2003JA010150.

Mays, M.L., Taktakishvili, A., Pulkkinen, A., MacNeice, P.J., Rastätter, L., Odstrcil, D., Jian, L.K., Richardson, I.G., LaSota, J.A., Zheng, Y., 2015. Ensemble Modeling of CMEs Using the WSA-ENLIL+Cone Model. solphys 290, 1775–1814. doi:10.1007/s11207-015-0692-1, arXiv:1504.04402.

McComas, D.J., Elliott, H.A., Schwadron, N.A., Gosling, J.T., Skoug, R.M., Goldstein, B.E., 2003. The three-dimensional solar wind around solar maximum. Geophysical Research Letters 30. doi:10.1029/2003GL017136.

Meyer-Vernet, N., 2007. Basics of the Solar Wind. Cambridge Atmospheric and Space Science Series, Cambridge University Press. URL: https://books.google.co.uk/books?id=qZK6ngEACAAJ.

Mignone, A., Bodo, G., Massaglia, S., Matsakos, T., Tesileanu, O., Zanni, C., Ferrari, A., 2007. PLUTO: A Numerical Code for Computational Astrophysics. apjs 170, 228–242. doi:10.1086/513316, arXiv:astro-ph/0701854.

Odstrcil, D., 2003. Modeling 3-d solar wind structure. Advances in Space Research 32, 497 – 506. doi:https://doi.org/10.1016/S0273-1177(03)00332-6. heliosphere at Solar Maximum.

Odstrcil, D., Pizzo, V.J., 1999. Three-dimensional propagation of coronal mass ejections (cmes) in a structured solar wind flow: 1. cme launched within the streamer belt. Journal of Geophysical Research: Space Physics 104, 483–492. doi:10.1029/1998JA900019.

Owens, M.J., Forsyth, R.J., 2013. The heliospheric magnetic field. Living Reviews in Solar Physics 10, 5. URL: https://doi.org/10.12942/lrsp-2013-5, doi:10.12942/lrsp-2013-5.

Parker, E.N., 1965. The passage of energetic charged particles through interplanetary space. Planetary and Space Science 13, 9–49. doi:10.1016/0032-0633(65)90131-5.

Parsons, A., Biesecker, D., Odstrcil, D., Millward, G., Hill, S., Pizzo, V., 2011. Wang-sheeley-argecenlil cone model transitions to operations. Space Weather 9. doi:10.1029/2011SW000663.

Pomoell, J., Poedts, S., 2018. EUHFORIA: European heliospheric forecasting information asset. Journal of Space Weather and Space Climate 8, A35. doi:10.1051/swsc/2018020.

Powell, K.G., Roe, P.L., Linde, T.J., Gombosi, T.I., Zeeuw, D.L.D., 1999. A solution-adaptive upwind scheme for ideal magnetohydrodynamics. Journal of Computational Physics 154, 284 – 309. URL: http://www.sciencedirect.com/science/article/pii/S002199919996299X, doi:https://doi.org/10.1006/jcph.1999.6299.

Riley, P., Caplan, R.M., Giacalone, J., Lario, D., Liu, Y., 2016. PROPERTIES OF THE FAST FORWARD SHOCK DRIVEN BY THE 2012 JULY 23 EXTREME CORONAL MASS EJECTION. The Astrophysical Journal 819, 57. doi:10.3847/0004-637x/819/1/57.

Riley, P., Lionello, R., Linker, J.A., Mikic, Z., Luhmann, J., Wijaya, J., 2011. Global MHD Modeling of the Solar Corona and Inner Heliosphere for the Whole Heliosphere Interval. solphys 274, 361–377. doi:10.1007/s11207-010-9698-x.

Russell, C., Priest, E., Lee, L., Union, A.G., 1990. Physics of Magnetic Flux Ropes. Geophysical Monograph Series, Wiley. URL: https://books.google.co.uk/books?id=cJORAQAAIAAJ.

Savage, S.L., McKenzie, D.E., Reeves, K.K., Forbes, T.G., Longcope, D.W., 2010. RECONNECTION OUTFLOWS AND CURRENT SHEET OBSERVED WITHHINODE/XRT IN THE 2008 APRIL 9 "CARTWHEEL CME" FLARE. The Astrophysical Journal 722, 329–342. doi:10.1088/0004-637x/722/1/329.

Smith, E.J., 2001. The heliospheric current sheet. Journal of Geophysical Research: Space Physics 106, 15819–15831. URL: https://agupubs.onlinelibrary.wiley.com/doi/abs/10.1029/2000JA000120, doi:10.1029/2000JA000120.

Thomas, B.T., Smith, E.J., 1981. The structure and dynamics of the heliospheric current sheet. Journal of Geophysical Research 86, 11105–11110. doi:10.1029/JA086iA13p11105.

Tsurutani, B.T., Gonzalez, W.D., Lakhina, G.S., Alex, S., 2003. The extreme magnetic storm of 1-2 September 1859. Journal of Geophysical Research (Space Physics) 108, 1268. doi:10.1029/2002JA009504.

Wood, B.E., Howard, R.A., 2009. AN EMPIRICAL RECONSTRUCTION OF THE 2008 APRIL 26 CORONAL MASS EJECTION. The Astrophysical Journal 702, 901–910. doi:10.1088/0004-637x/702/2/901.